Soft Matter

Accepted Manuscript

ROYAL SOCIETY OF CHEMISTRY

www.rsc.org/softmatter

Bubbles and foams in microfluidics

Axel Huerre,[‡] **Vincent Miralles,**[‡] **and Marie-Caroline Jullien**[*]

Received Xth XXXXXXXXXX 20XX, Accepted Xth XXXXXXXXX 20XX
First published on the web Xth XXXXXXXXXX 200X
DOI: 10.1039/b000000x

Microfluidics offers great tools to produce highly-controlled dispersions of gas into liquid, from isolated bubbles to organized microfoams. Potential technological applications are manifold, from novel materials to scaffolds for tissue engineering or enhanced oil recovery. More fundamentally, microfluidics makes it possible to investigate the physics of complex systems such as foams at scales where the capillary forces become dominant, in model experiments involving few well-controlled parameters. In this context, this review does not have the ambition to detail in a comprehensive manner all the techniques and applications involving bubbles and foams in microfluidics. Rather, it focuses on particular consequences of working at the microscale, under confinement, and hopes to provide insight into the physics of such systems. The first part of this work focuses on bubbles, and more precisely on *i)* bubble generation, where the confinement can suppress capillary instabilities while inertial effects may play a role, and *ii)* bubble dynamics, paying special attention to the lubrication film between bubble and wall and the influence of confinement. The second part addresses the formation and dynamics of microfoams, emphasizing structural differences from macroscopic foams and the influence of the confinement.

1 Introduction

The field of droplet/bubble-based microfluidics has garnered a lot of interest over the past few years. As often in microfluidics, the potential for many technological applications coexists with the advantages of such microdevices to design model experiments with a small number of well-controlled parameters, allowing the investigation of complex problems at scales hardly accessible in the past. Many reviews have reported on the achievements of digital microfluidics to overcome experimental challenges and bring fundamental understanding[1–5], while a large variety of applications can be cited, from new materials (phononic[6], photonic[7,8], tissue engineering[9–11]), labs-on-a-chip[1] (bioanalytical applications[12], pharmaceutics[13,14], environment[15]), to enhanced oil recovery (EOR)[16–18]. The step from isolated bubbles to close-packed foams is one technically easy to take in such devices, and discrete microfluidics (so-called to differentiate it from individual bubbles set-ups[19]) offers in its turn a wealth of fundamental and technical applications. Microfluidic foams can be used to build new materials such as scaffolds for tissue engineering, microporous media, optics and phononic crystals. To cite one example, 2D phononic crystals formed from gas microinclusions in a PDMS matrix show an interesting response to ultrasonic frequencies, with deep transmission minima[6,20]: microfluidics should help generate such materials, with good control over their physical properties, e.g. through the geometry of the gas inclusions.

The present work reports on the generation and dynamics of bubbles and foams in confined microgeometries. Precisely, we focus on bubbles with a free surface, *i.e.* there is always a wetting film between bubble and walls: segmented flows with a triple line are out of the scope of this review[2,21–23]. In particular, we stress throughout the review the influence of the confinement, as well as some specificities of working at the microscale. Though micro-droplets have been much investigated, the literature on micro-bubbles and, even more so, micro-foams remains comparatively scarce. Yet the experimental potential of microfluidics is raising interest in the foam community, and we wish to provide a general picture that illustrates this potential and emphasizes some specific properties. Though we do not ambition to comprehensively list all the technical achievements, we mention a few examples and hope that this work will also prove useful for applicative purposes.

To recall the general picture of the physics at such scales, Table 1 provides the typical range of relevant hydrodynamic dimensionless numbers in microfluidic experiments. The low values of the Reynolds (comparing inertial to viscous forces), Weber (inertial to capillary forces), Bond (gravity to capillary forces) and capillary (viscous to capillary forces) numbers indicate that surface tension and viscous forces should dominate in microfluidics. However, we shall see in the following that inertial forces cannot always be disregarded. Note that we sometimes refer to millifluidic experiments, which involve confinements ranging from 0.5 mm to 2 mm. We will see below that similar behaviors are expected for both micro- and millifluidics as long as the confinement is below the capillary length. In the first part of this review, we focus on isolated bubbles: after looking at the consequences of confinement

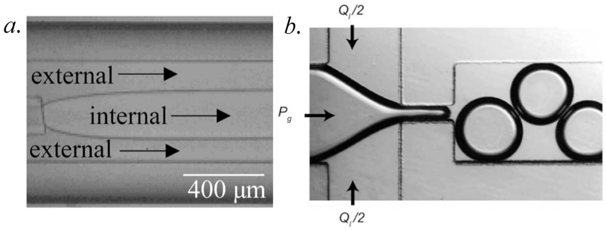

Fig. 1 a: Microfluidic co-flowing junction. Reprinted with permission from [39]. Copyright 2007 by the American Physical Society.**b:** Flow-focusing of a gas jet by liquid streams into an orifice of width 100 μm. Reprinted with permission from [30].Copyright 2009, Royal Society of Chemistry.

on bubble generation, we go over developments in the understanding of bubble dynamics in confined channels since the pioneering work of Bretherton[24–28]. The second part focuses on foams and reviews how the microscales can affect their geometry, how bubbles organize at such scales, and what their flow properties are, extending the results obtained for single bubbles.

2 Isolated bubbles

2.1 Generation

Microfluidic devices can allow for high-throughput production of bubbles with very well-controlled size and generation frequency: as fast as 100 Hz, with diameters ranging from 10 to 500 μm, and a polydispersity lower than 5 %[7,31,32]. The typical geometries involved, such as the T-junction[33–36], the flow-focusing junction[32,37,38](Fig. 1(b)), the co-flowing junction[39,40] (Fig. 1(a)), the liquid cross-flow[41] or the 2.5D geometry[42] are now well-known implements in the microfluidics toolbox. The formation of bubbles/droplets has been extensively investigated, published and reviewed, taking into account various parameters such as the viscosity ratio, flow rates, gas pressure, channel geometry, channel wettability (to cite a few)[1–3,37]. In this context, we wish to specifically underline some points of interest in the generation of bubbles in some of the above-mentioned geometries, with a particular focus on situations where the confinement by the channel walls plays a role.

The general picture for bubble generation in flow-focusing and T-junction geometries is that the dispersed phase blocks the outlet channel so that the upstream pressure in the liquid phase builds up and pinches the dispersed phase. Garstecki *et al.* suggested that the breakup proceeds through a series of equilibrium states[37]; such a scenario for breakup in a T-junction has been confirmed in numerical simulations[35] for droplets at small Ca ($< 10^{-2}$). In such configurations, breakup is driven by normal stress instead of tangential stress.[†] However, a closer look at various bubble generation mechanisms reveals further subtleties.

At such small Ca, capillary phenomena are expected to be dominant over hydrodynamic forces. However, the presence of the walls tends to stabilize capillary instabilities. Guillot *et al.* studied the stability of a jet produced in a co-flowing junction (Fig. 1(a)), in different geometries: axisymmetric[39], or with a rectangular channel cross-section[29]. In this situation, reminiscent of the Rayleigh-Plateau instability, they showed via linear stability analysis that the jet is always unstable in the axisymmetric geometry, and identified the three main parameters at play: the capillary number, the viscosity ratio between the two phases, and the confinement (the ratio of the jet radius to the channel radius). They quantified two distinct instability regimes. For low inner-phase flowrates, the instability is absolute: it propagates upstream and downstream, and the inner phase breaks up into droplets at the nozzle, whereas for large inner phase flowrates, the instability is convected downstream and a continuous jet is maintained over a distance. In this geometry, bubble formation is due to the interplay between capillarity forces and viscous friction, and they note that increasing the confinement leads to a decrease of the rate of development of perturbations. However, if the channel cross-section is rectangular instead of axisymmetric, the confinement can stabilize the jet, preventing perturbations from developing once the jet width becomes comparable to the smallest dimension of the section. Bubble formation was also investigated with an analogous theoretical approach in a flow-focusing geometry[43]. Varying the section aspect ratio at the flow-focusing orifice, Dollet *et al.* observed two regimes over time (Fig. 2): *i)* in the first regime, the width of the gas thread thins but remains larger than the channel height, corresponding to what they call a 2D collapse, until *ii)* the gas thread is thin enough to become 3D, and the collapse is driven by inertia. The higher the aspect ratio of the channel cross-section, the longer the liquid thread spends in the 2D regime. This is of particular interest for bubble generation purposes: the 2D regime is always stable as fluctuations are dissipated by the outer phase viscosity, and spending a long time in this regime leads to a good bubble monodispersity. Conversely, the 3D regime is always unstable, which limits reproducibility and leads to polydispersed bubbles, but reaching it faster allows for higher production

---

Gulliver CNRS ESPCI ParisTech, UMR 7083, MMN, 10 rue Vauquelin, 75005 Paris, France. Fax: +33-1-40-79-51-61; Tel: +33-1-40-79-51-57; E-mail: marie-caroline.jullien@espci.fr

‡ These authors contributed equally to this work

[†] At larger capillary numbers in a T-junction, the dispersed phase does not block the outlet channel anymore and the bubble size results from a competition between interfacial tension and viscous stress, and thus depends on the capillary number.

Table 1 Typical values of the problem parameters and their associated relevant numbers

Parameters		Relevant numbers	
Parameter: symbol	Typical values	Definition	Orders of magnitude
Liquid viscosity: η	10^{-3} - 1 Pa.s	Capillary number: $Ca = \eta U/\gamma$	10^{-7} - 10^{-1}
Bubble velocity: U	10 - 1000 μm.s^{-1}	Reynolds number: $Re = \rho UL/\eta$	10^{-5} - 10^{-1}
Surface tension: γ	20 - 70 mN.m^{-1}	Bond number: $Bo = \rho g L^2/\gamma$	10^{-5} - 10^{-1}
Length scale: L	10 - 500 μm	Weber number: $We = \rho U^2 L/\gamma$	10^{-11} - 10^{-5}
Fluid density: ρ	10^3 kg.m^{-3}	Capillary length: l_c	2 mm

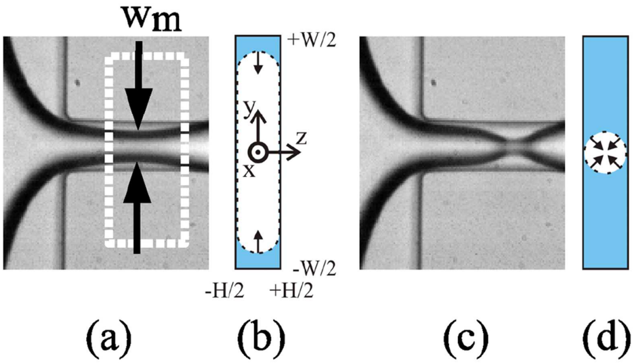

Fig. 2 Snapshots of the gas thread during collapse in a flow focusing junction, for a given channel aspect ratio. **a-b:** 2D collapse at short times, top view and sketch of the cross-sectional view; **c-d:** 3D collapse, top view and sketch of the cross-sectional view. Reprinted with permission from [43]. Copyright 2008 by the American Physical Society.

frequencies. This result is in agreement with previous works, which predicted the bubble volume to depend on the flow parameters and not the capillary number for flow-focusing or T-junctions[32–34,36,37].

Recently, Van Hoeve *et al.*[44] shed more light on the effect of inertia on bubble pinch-off. They studied the collapse of a gaseous thread in a liquid, in a flow-focusing geometry. Using a videocamera at 1 Mfps, the authors could investigate the bubble collapse with an impressive time resolution, which allowed them to follow the evolution of several parameters, such as the two neck radii of curvature, the bubble volume and the gas velocity. At short times, the gas at the neck is replaced by liquid due to a pressure gradient in the continuous phase. The collapse is induced by this filling effect and is driven by surface tension and viscosity, which leads to a neck radius scaling as $\tau^{1/3}$, where $\tau = t_c - t$ (t_c is the collapse time), consistently with previous observations[43,44]. Close to pinch-off, the 3D collapse can be accounted for by solving the Rayleigh-Plesset equation, taking into account viscosity and surface tension. By mapping the different pressure contributions over time, they find that the pinch-off is mainly driven by inertia in the liquid phase, even though surface tension is non negligible; in this regime the neck radius scales as $\tau^{2/5}$, consistently with their experimental results.

Above a critical flow rate, two bubbles of different sizes are produced within one period[32]. As the flowrate increases (over a range of Ca from 10^{-4} to 10^{-1} and We from 10^{-4} to 10^2), the period doubling is followed by cascades of period doubling and chaotic bubbling[45].

The fact that capillary instabilities can be suppressed under micro-confinement has important consequences on bubble generation, as seen above, but also on bubble/droplet breakup. Leshansky *et al.* theoretically investigated the breakup of bubbles in a T-junction in a 2D geometry[46,47]. They postulated that instabilities such as Rayleigh-Plateau cannot emerge in such a finite medium. Instead, a bubble breaks (or not) depending on its initial extension and on the capillary number. Their model is based on the geometry of the interface shape, coupled to a lubrication analysis in a narrow gap where the surface tension competes with the viscous drag. Experimental results are in good agreement with this theoretical approach in the case of droplets[48], though the prefactors are slightly different and seem to depend on the viscosity ratio, a parameter that should be taken into account in the models; however the scalings are recovered. The fact that a 2D model manages to capture the main features of 3D experiments suggests that the flow in the gutters, *i.e.* the continuous phase that bypasses the bubble in the corners of the rectangular channel, Fig. 3(b), does not play a significant role. To our best knowledge this question has not yet been addressed.

Bubble generation is also affected by the presence of surfactants that can rigidify interfaces[49–51]; such surfactants are, for instance, often used in the development of ultrasound contrast agents in order to avoid gas dissolution into the continuous phase[13,14]. Surfactants can be more or less soluble in water (down to insoluble). This affinity for water affects their adsorption and desorption rates. For example, an insoluble surfactant has a high desorption time (compared to classic advection times) and thus moves with the interface without desorbing into the bulk. This property leads to different possible boundary conditions for the interface: respectively mobile/immobile for soluble/insoluble surfactants (the second case leading to a rigidified interface)[26,27,50,52]. Van Hoeve *et*

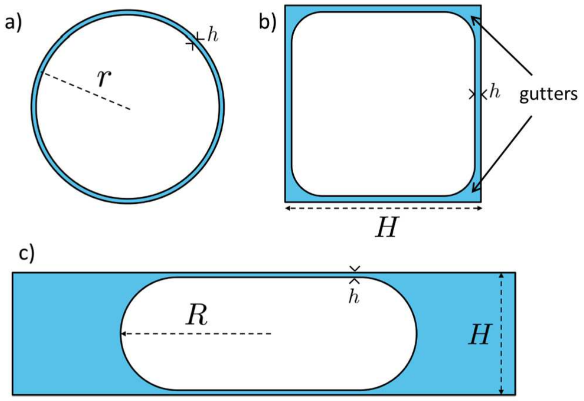

Fig. 3 Schematics of the common geometries used to study the flow of confined bubbles. **a:** round capillary; **b:** rectangular channel (here with a square cross section); **c:** Hele-Shaw cell. The liquid phase is represented in blue, the gas in white. There is a lubrication film of thickness h between the bubble and the walls.

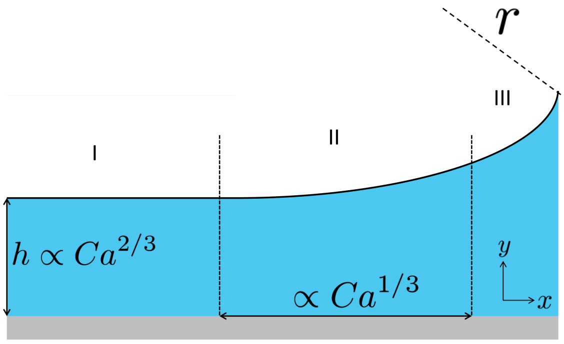

Fig. 4 Schematics of the bubble profile at the front meniscus. Zone I: constant thickness zone, zone II: dynamical meniscus, zone III: cap region. Scaling laws are given for the thickness h or the spatial extension of specific zones[24].

al. studied theoretically the size of bubbles generated from a gaseous cylindrical jet in a co-axial geometry[40], and found a small variation due to the change in boundary condition at the interface. Without surfactant, *i.e.* with shear stress continuity at the interface, they predict that the bubble radius should scale as $R \sim \tilde{Q}^{5/12}$ with the flow rate ratio between the two phases, for $\tilde{Q} \equiv Q_g/Q_l < 1$. This scaling is modified by the presence of high molecular weight surfactants that rigidify the interface and change the boundary condition. The discontinuity of the shear stress at the rigid interface leads to different velocity profiles in the dispersed phase, which affects the bubble radius: $R \sim \tilde{Q}^{1/2}$.

2.2 Dynamics

The problem of a single confined bubble pushed by a viscous fluid has been addressed since the late 50s and is still not fully understood. Efforts have been made to rationalize this issue from a theoretical point of view, and numerical developments allow for the prediction of velocities with a great accuracy. From the experimental perspective, microfluidic techniques have made it possible to handle small and reproducible fluid volumes in perfectly known confined geometries. Many recent experiments have been focusing on the dynamics of a single bubble traveling in a confined geometry, with a typical lengthscale under 1mm.

2.2.1 General framework. The first theoretical approach to understanding the behavior of a bubble pushed by its surrounding fluid is the classic work of Taylor and Saffman in 1959[53]. In their historical paper, they considered an air bubble moving in a water phase in a Hele-Shaw geometry, as sketched in Fig. 3(c). Their analysis is based on a potential flow and the bubble is assimilated to a cylinder occupying the whole height of the cavity: there is no meniscus or water film between the bubble and the walls, and all the dissipation occurs in the liquid phase around the bubble, where the equations can be averaged over the height of the cell due to confinement. This first model leads to a family of possibilities for the velocity and shape of the bubble, but experiments showed that the solution is unique for a given outer fluid velocity. Minimizing the product of the parameters leads to a bubble velocity $U = 2V$, where V is the carrier fluid velocity: though not based on physical arguments, this solution was in good agreement with the experiments at that time.

The presence of a thin film of water between the bubble and the wall and its influence on bubble velocity was first investigated by Bretherton in 1961[24]. He understood that viscous dissipation can occur in this lubrication film, so that knowing the shape of the interface is necessary to determine the bubble velocity. In this seminal work, a bubble is squeezed in a thin round capillary and pushed by a viscous fluid, Fig. 3(a). The capillary radius r is small enough that the corresponding Reynolds and Bond numbers are very small; as the bubble travels along the capillary, a thin film of thickness h is left by the advancing meniscus. The profile of the bubble can be divided into two main regions, see schematics in Fig. 4: the cap region (zone III), where the surface tension dominates, and the inner film region (zones I and II), where viscous dissipation and surface tension forces are of the same order of magnitude. The film thickness h is constant in zone I, and is set by the radius of the capillary r and Ca. In zone II, referred to as the *dynamical meniscus* in reference to

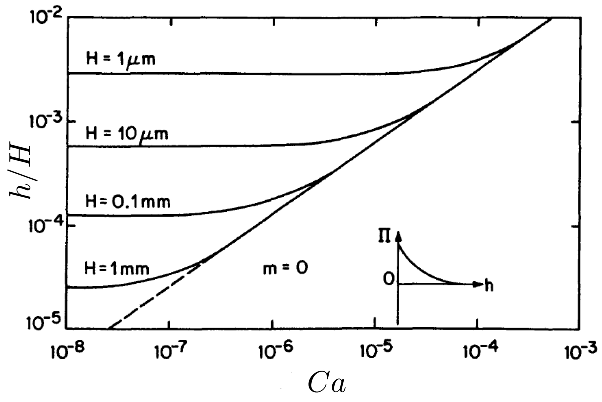

Fig. 5 Dependence of the dimensionless film thickness with the capillary number and tube radius H. Reprinted with permission from [28].

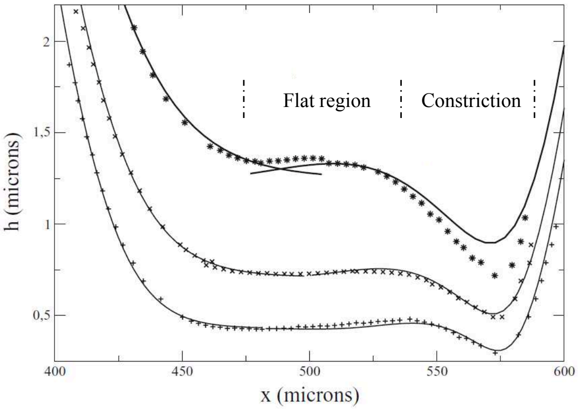

Fig. 6 Lubrication film profiles for a confined bubble at different Ca. h increases with Ca. The bubble travels from right to left, notice the constriction at the rear meniscus. Dots are extracted from experiments[60] and full lines are theoretical curves. Reprinted with permission from[27]. Copyright 2013, AIP Publishing LLC.

the Landau-Levich theory[54], the viscous stress modifies the static profile at small Ca. A prediction for h is obtained by solving the Stokes equations ($Re \ll 1$, stationary, no external forces) in the lubrication approximation (small slope, only y-derivatives), with boundary conditions of zero tangential stress at the interface and no slip at the wall, and adding the flux conservation: $h_{\text{Breth}}/r = 0.643(3Ca)^{2/3}$, where r is defined in Fig. 3(a) and Fig. 4[24]. In turn, the pressure drop due to the presence of the bubble is $\Delta P = 3.58(3Ca)^{2/3}\gamma/r$, and the velocity ratio is $U/V = 1/(1-1.23\,(3Ca)^{2/3})$. In the following, we review later refinements of this result, paying particular attention to how the geometry of the channel (shape of the cross-section, curvature and height variations along the channel) affects the bubble dynamics, as well as the influence of surfactants at the interface.

In the case of droplets, numerical simulations taking into account the inner phase viscosity as well as intermolecular forces in the lubrication films recovered Bretherton's scalings, for both round capillaries and Hele-Shaw cells[28,55]. However, a new dynamical regime was uncovered at very low Ca, in which the film thickness is entirely determined by the disjoining pressure[28,56] (in the case of repulsive forces). In this regime, h plateaus at an asymptotic value set by the intermolecular forces, see Fig. 5. To our knowledge, this was never investigated experimentally, but it should have consequences in microfluidics since the typical parameter range should allow reaching this regime, Fig. 5. For instance, $Ca = 10^{-6}$ and $r = 100\ \mu$ m give $h_{\text{Breth}} \approx 10$ nm, while surface interactions should be felt over about ≈ 100 nm. On a different note, these studies also evidenced the presence of a stagnation point at the surface of the bubble, which position depends on $\tilde{\eta}$, the viscosity ratio between the two phases, and Ca. This stagnation point generates a counter flow in the liquid phase, and these recirculations can be put to use for mixing purposes[57] (which is a challenge at such low Reynolds numbers[58]).

The fact that Bretherton's prediction holds for a Hele-Shaw geometry is not surprising, considering that, for $R \gg H$ (see Fig. 3(c)), the Hele-Shaw and round capillary geometries are similar in first approximation. Using two small parameters, $Ca^{1/3}$ and a characteristic length in the z-direction to account for a 3D effect, a double Taylor expansion of Bretherton's equations recovers the same scaling law for the film thickness at the first order in $Ca^{1/3}$ with no corrections to add at the second order, while the third dimension plays no role at least for the first two orders[59].

A different approach consists in solving numerically the shape of the meniscus from an arc-length formulation of the lubrication equation[61]. Treating the problem like a dynamical system with three variables (pressure, curvilinear abscissa and angle) yields trajectories in the phase space that represent possible bubble shapes. The right profile for the film and dynamical meniscus is chosen by imposing the shapes of the front and rear static menisci as boundary conditions. For round capillaries, this technique extends the analysis of Bretherton to higher Ca and finite bubbles, as long as their length exceeds the radius of the capillary. Profiles are obtained for the menisci by solving Bretherton's equations at the front, and the problem of a meniscus flowing on a static film of known thickness at the rear. This major difference leads to the formation of a constriction at the end of the bubble, see Fig. 6. This analysis can be extended to the Hele-Shaw geometry[25]. In the schematics in Fig. 7, the different scalings are illustrated for half a bubble. When going from the sides to the center, one crosses successively the capillary-static region (zone III), the transi-

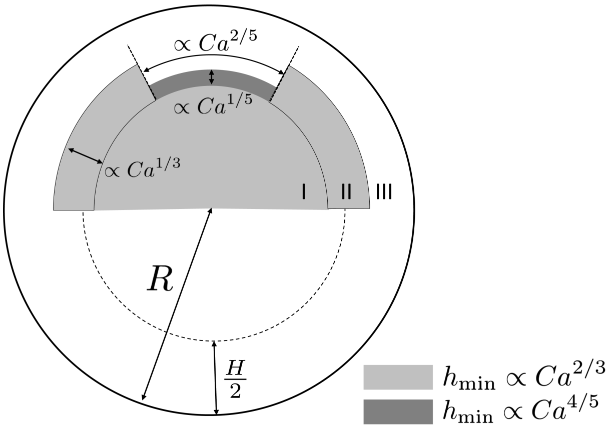

Fig. 7 Top view of a bubble in a Hele-Shaw cell. Zones I, II and III stand for the corresponding regions in the film profile in a round capillary, Fig. 4. The light gray area follows Bretherton's scaling with an asymptotic value $\propto Ca^{2/3}$. The dark gray lateral area corresponds to a constriction with a minimum thickness $\propto Ca^{4/5}$. Scalings for the spatial extensions are also provided. Adapted with permission from[25]. Copyright 1990, AIP Publishing LLC.

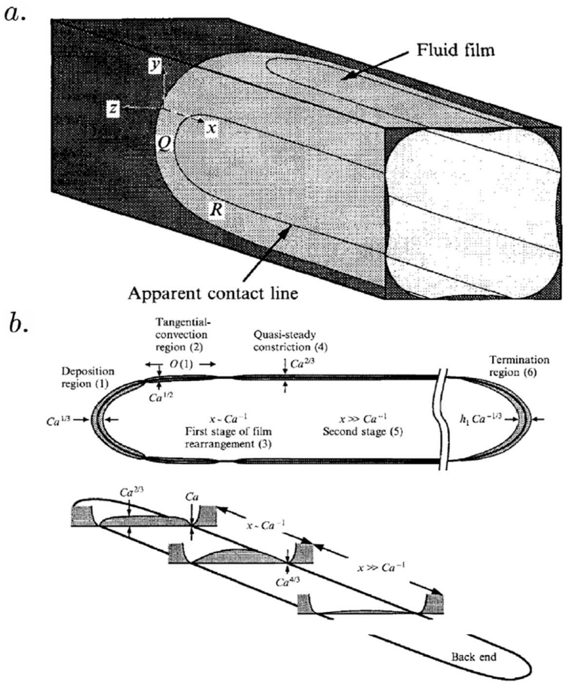

Fig. 8 a: 3D view of the bubble profile in a square channel. **b:** Shape of an elongated bubble in a rectangular channel. Top: Schematic view of the bubble with the different regions and their spatial extensions. The bubble travels from right to left. Bottom: View of the constrictions and scaling laws in the different regions. Reprinted with permission from [62].

tion region with changes in scaling depending on the lateral position (zone II) and the thin film region (zone I). This approach recovers Bretherton's result for the region of constant h in the main part of the bubble (light gray, $h \propto Ca^{2/3}$), and a constriction in the side region (dark gray), where the minimum film thickness scales as $Ca^{4/5}$. Theoretical and numerical results of this problem were recently reviewed by Cantat[27], with a good experimental agreement for the film profiles[60] (Fig. 6).

Interestingly, the profile of the meniscus in rectangular channels was shown to be qualitatively different[62]. In this case, the shape of the dynamical meniscus (and, consequently, the dissipation) depends on the length of the bubble and Bretherton's scaling for the film thickness is lost. Three different regions are identified along the bubble axis, see Fig. 8(b). In the deposition region at the front of the bubble, the lubrication layer is a flat Bretherton's film with particular boundary conditions in the transverse direction to match the curvature imposed by the corners. This flat film turns into a parabolic profile in the second region, at $x = H\, Ca^{-1}$. Towards the rear of the bubble, for $x \gg H\, Ca^{-1}$, the film thins as the continuous phase leaks into the corners of the channel (see Fig. 8(b) for the respective scalings, and Fig. 8(a) for the final shape of the bubble[62]). In calculating the drag force, a difference from the axisymmetric case arises from curvature rearrangements in the film at the rear of the bubble, but the force essentially scales like $Ca^{2/3}$ whatever the bubble length and geometry (which affect the numerical prefactors)[62]. Hence, the classical scaling law for the pressure drop, $\Delta P \propto Ca^{2/3}$, is maintained, at the exception of very low Ca ($\approx 10^{-8}$), where corner flows predominate and the pressure drop follows $\Delta P \propto Ca$. However, such a regime is rarely reached in typical experimental conditions in microfluidics.

Finally, note that the pressure drops can reach significant values in microfluidics (typically around a few kPa). Because of the gas compressibility, this can lead to the volumetric expansion of the bubbles, depending on the channel length[63–65].

2.2.2 Influence of surfactants. As a strong effort was put into the experimental validation of the previous theories, models had to be refined to account for the presence of impurities or surfactants in a number of these experiments. Whether the model concerned a small amount of impurities[61](concentration gradient in the bulk) or a concentrated solution[52](where the mass transfer is adsorption-controlled), it was shown that the higher the concentration, the thicker the lubrication film. The values for h are bounded between the clean surface expression derived by Bretherton and an upper limit of $4^{2/3}\ h_{\mathrm{Breth}}$, which corresponds to no flow in the film, *i.e.* zero interface velocity: this is referred to as the *rolling case*. The pressure difference follows the same trends. An interesting point to raise is the fact that the surfactants can modify the rheology of the interface and the associated boundary

Table 2 Scaling laws for h, ΔP and U/V depending on the mobility of the surfactant. The corresponding references are indicated into brackets.

	Mobile	Immobile
h	$h_{\text{Breth}} = 0.67\ r\ Ca^{2/3}$ [24,27,66,67]	$2^{2/3}\ h_{\text{Breth}}$ [27,68]
ΔP	$\beta_1\ Ca^{2/3}$ [27]	$\beta_1\ Ca^{2/3} + \beta_2\ Ca^{1/3}$ [27]
$\frac{U}{V}$	$\propto Ca^{1/3}$ [66] $\frac{2}{1+\beta_1\ H/R\ Ca^{-1/3}}$ [67]	$\frac{2}{1+0.182\ Ca^{-2/3}}$ [68] $\frac{2}{1+\beta_1\ H/R\ Ca^{-1/3}+\beta_2\ Ca^{-2/3}}$ [67]

condition[26,27]. In the *sliding case*, where the velocity of the interface is equal to the bubble velocity, the dissipation occurs both in the lubrication films and the menisci[26,27]. This leads to $\Delta P \propto \beta_1\ Ca^{2/3} + \beta_2\ Ca^{1/3}$, where β_1 and β_2 are constants, and the two terms account respectively for the dissipation in the menisci and in the films.

Though the previous experiments concerned round capillaries, similar results were obtained in Hele-Shaw configurations. A first discrepancy with the prediction by Saffman and Taylor was observed for large bubbles flowing in glycerin solutions in a Hele-Shaw cell[69]. For circular bubbles (in top view), the measured velocity was $U = 0.2V$; this difference was attributed to the possibly three-dimensional nature of the flow. To solve this velocity inconsistency, Maruvada *et al.*[68] took into account the rigidification of the interface due to surfactants, and found $h = 2^{2/3} h_{\text{Breth}}$ for a rigid surface (sliding case). Assuming the bubble to be elliptic, they derived $U/V = (k+1)/(1+0.2\,k\,I\,Ca^{-2/3})$, where I is a definite integral that accounts for the film thickness variation in the transverse direction, and k is a shape factor. This expression becomes $U/V = 2/(1+0.182\,Ca^{-2/3})$ for circular bubbles, in good agreement with their millifluidic experiments for $[c]_{\text{SDS}} <$ cmc, where cmc is the critical micelle concentration. Recently, a different expression for the bubble velocity was introduced by Rabaud *et al.*, who performed microfluidics experiments in which they flowed bubbles in a Hele-Shaw geometry[66]. They modeled the drag force as the sum of a viscous drag (liquid on bubble) and a friction force (bubble on wall), where the scaling law for the friction force is derived from Bretherton arguments, considering that the dissipation occurs in the dynamical meniscus. This yields an expression with two unknown parameters for the drag force, a_{wall} and a_{fluid}, which can be estimated experimentally by balancing the drag force with buoyancy. Following the analysis gives in turn a velocity ratio $U_x/V \propto a_{\text{fluid}}/a_{\text{wall}} \times Ca^{1-\alpha}$, where $1/2 < \alpha < 2/3$ reflects the mobility of the surfactant and U_x is the axial velocity, with a very good experimental agreement. The power law discrepancy with the previous result[68] is attributed to the friction area (related to the dynamical meniscus), considered to be non constant with the velocity. Lastly, an expression for the bubble velocity was derived analytically from a comprehensive model in Dangla's PhD thesis (not yet published)[67]. They find $U/V = 2/(1+\beta_1\,H/R\,Ca^{-1/3} + \beta_2\,Ca^{-2/3})$, where β_1 and β_2 are constants. The relative values of β_1 and β_2 reflect the surfactant ability to rigidify the interface ($\beta_2 \neq 0$) or not ($\beta_2 = 0$)[66]. Table 2 provides the scaling laws for h, ΔP and U/V depending on the mobility of the surfactant.

A situation more representative of typical microfluidics experiments is a succession of bubbles traveling trough a rectangular channel, separated by slugs of continuous phase. The influence of the surfactant concentration on the pressure drop was investigated in this configuration by separating three zones: the gutters Fig. 3(b), the curved caps at the front and rear of the bubbles, and the liquid slugs between bubbles[70]. Assuming that the film flows are negligible compared to the corner flows, the expression for the pressure drop writes $\Delta P \propto \gamma/H[\beta_1\ Ca^{2/3} + Ca/H(\chi_1\ d_{\text{bubbles}} + \chi_2\ L_{\text{film}})]$, where d_{bubbles} is the distance from cap to cap between two following bubbles, L_{film} is the length of the film region, and χ_1 and χ_2 are constants. Experimental observations show that the surfactant concentration affects the relative importance of the terms in this expression. If $[c] <$ 0,1cmc or $[c] \gg$ cmc, the first term dominates as the dissipation mainly occurs in the cap regions, and the classical scaling holds. However, for intermediate concentrations, dissipation in the gutters plays a significant role and the second term becomes non negligible, consistently with previously mentioned results in a rectangular channel[62]. This can be understood as the competition between adsorption/desorption and convection of the surfactant along the interface. At intermediate concentrations, a surfactant concentration gradient builds from the front to the rear, resulting in a pressure drop and the associated flow in the gutters. This notably affects the bubble velocity, as bubbles are much slower for intermediate concentrations of surfactants: in this case experimental measurements find $U/V = 0.47$ instead of $U/V = 0.83$ at small or high concentrations[70].

Lastly, in Teletzke *et al.*[28], the authors briefly evoked the possibility of surfactant concentration gradients that could account for the discrepancy between theoretical and experimental film thicknesses. According to these authors, the concentration is maximum at the tip because of the presence of a stagnation point and its associated reverse flow, while the minimum lies somewhere in the transition region. This Marangoni-induced counter flow could explain the thicker observed film.

2.2.3 Geometrical effects along the channel. Modifying the channel geometry along its length has interesting consequences on bubble dynamics. For instance, curvature along the length of the channel speeds the bubbles up relatively to

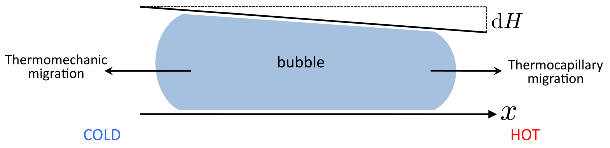

Fig. 9 Mechanisms involved in the migration of a bubble under a temperature gradient. Thermocapillarity drives the bubble towards the lower surface tension area, *i.e.* towards the high temperatures for air in water + SDS at the cmc. The temperature-induced dilation of PDMS drives the bubbles towards the cold side, where the bubble can adopt a minimum surface area. Reprinted with permission from[74]. Copyright 2011, AIP Publishing LLC.

the outer phase velocity (and the corresponding straight channel). More precisely, it was shown numerically that the relative bubble velocity increases monotically with the channel curvature, for circular or square cross-sections[71]. Numerical simulations showed that the lubrication film is thinner on the inside of the bend than on the outside. Using different radii to take this into account, an analysis similar to Bretherton's yields $h_o = h_i\,(1+w/R_i)^{5/3}$, where the subscripts o and i stand for outer and inner; w is the width of the channel and R_i is the inner radius of curvature.

Another example is the influence of thickness variations along the channel on bubble mobility. Microfluidic experiments often rely on soft lithography and the use of elastomers such as PDMS as channel material. However, PDMS can swell when exposed to certain solvents or temperature variations, deforming the channels; this in turn will lead to deviations in droplet/bubble trajectories[72]. However, it is possible to take advantage of PDMS dilation in a controlled manner in order to propel bubbles. A thermomechanical effect was characterized by creating a well-controlled temperature gradient along such a microfluidic system[73,74]. The bubbles were observed to migrate towards the cold side, *i.e.* in a direction opposed to the expected one, due to the Marangoni flux balance towards the hot side. A very slight tilt in the wall (0.1 %), due to the temperature-induced dilation of the PDMS, is enough to counterbalance the thermocapillary migration (Fig. 9). Taking into account both contributions as well as the dissipation at the meniscus, the bubble velocity writes as: $|U| = \left|\frac{\gamma}{\eta}\left(\frac{R}{\xi}\right)^{3/2}\left(\frac{1}{H}\frac{\partial H}{\partial x} - \frac{1}{\gamma}\frac{\partial \gamma}{\partial x}\right)^{3/2}\right|$, where ξ is an adjustable parameter. It is worth noticing that the thermomechanical effect (corresponding to the second term in the expression) vanishes for an increasing cavity thickness, and classical thermocapillary migration is thus recovered for channels thicker than about 100 μm.

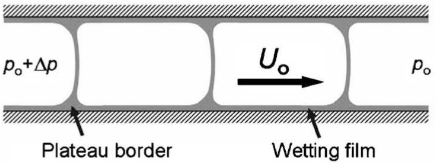

Fig. 10 Sketch of a bubble train. Reprinted with permission from[77]. Copyright 2006, AIP Publishing LLC.

2.2.4 Towards foams: increasing the bubble density.

Following this understanding of the physical mechanisms at play and inspired by the widely spread logic gates encountered in the fields of informatics or electronics, Prakash and co-workers[75] reported universal computation in an all-fluidic two-phase microfluidic system to do *microfluidic bubble logic*. The concept is simple: a bubble traveling in a channel represents a bit as well as the transportation of material (through AND/OR/NOT logic gates for instance), hence merging the fields of chemistry and computation. The collective dynamics of bubbles in microfluidic networks has also raised physical interest, as they constitute well-controlled model experiments of non linear collective behavior. Indeed, each bubble confined in a channel branch locally increases the hydrodynamic resistance of the network, affecting the trajectories of the following bubbles[76].

Increasing the bubble density leads to the formation of bubble trains (Fig. 10), *i.e.* lines of bubbles so closely packed that they are separated by a thin film of continuous phase. The static meniscus shape is different from the single bubble case, which in turns imposes different bubble shapes[61]. Surprisingly, no difference was found in the expression of the pressure drop. Another peculiar result is that the lubrication film around bubble trains is thinner in Hele-Shaw geometry than for a round capillary. In rectangular channels, bubble train dynamics were studied via a computational analysis using finite element methods[77]. Mapping the stress along the lubrication film showed that it was negligible compared to the stress in the menisci. The effect of the bubble size is quite negligible, provided that $L_{\mathrm{film}} > 10$ r Ca$^{1/3}$. Once the bubbles in such a train are packed close enough to be brought into contact, they form the simplest foam structure, the bamboo foam.

3 Foams

The structure of a foam can be characterized by two parameters: the volume fraction of the dispersed phase, ϕ_d, and the volume of the bubbles V_{bubble}. In wet foams, the bubbles maintain a spherical shape (or a pancake shape for a 2D foam). As the liquid fraction decreases, the bubbles are more close-packed and become faceted, separated by thin liquid films in dry foams.

3.1 Structure

3.1.1 Generation and stability. As we saw above, microfluidics offers several tools to generate bubbles with well-controlled volume, monodispersity, density or generation frequency, opening the way to a broad range of available foam geometries. Many bubble/foam lattices have been reported, their structure being controlled via the flow parameters and channel/nozzle geometry; a few examples are displayed in Fig. 11(a). To cite a few, T-junctions were used to create bubble pearl-necklaces, mono/polydisperse foams, 2D (with a single bubble layer) or 3D foams[34,41]. Flow-focusing devices led to bubbly flows, bamboo foams, packed foams, pancakes, or hexagonal structures with one, two or three rows in the direction transverse to the channel[30,32,78,79]. Well-controlled mono-, bi- and tri-disperse foams were even created using multi-flow-focusing devices[79].

Using geometrical arguments to account for the different nozzle geometries (T-junction, flow-focusing and co-flow) and different channel aspect ratios $\Lambda \equiv H/w$, Vuong and coworkers[78] established a complete phase diagram of the foam structure in the (ϕ_d, V^*) space (where $V^* = V_{\text{bubble}}/w^2H$ is the dimensionless bubble volume). An example of this diagram, obtained for $\Lambda = 0.2$, is shown in Fig. 11(b). The lines correspond to their numerical predictions for the transitions between the different regimes, and the symbols represent their experimental observations. It is readily shown that their approach reproduces the experimental observations. These phase diagrams give a global picture of the generation of structure-controlled foams and pave the way towards more complex issues, such as the generation of foam crystals or the 3D arrangements of such materials.

In order to stabilize the structure of a liquid foam, one has to control foam ageing, which involves three phenomena: *i)* the drainage of the liquid phase due to gravity, *ii)* the diffusion of gas through the liquid films, and *iii)* the coalescence of neighboring bubbles[80,81]. Note however that in the particular case of a 2D microfoam placed horizontally (*i.e.* $\vec{g}$ is parallel to the smallest dimension of the cavity), drainage due to gravity is negligible. Different strategies were devised to enhance bubble stability by counterbalancing or reducing these effects. A first strategy is to coat the bubbles with particles of adsorption and desorption energies much larger than k_BT[82–84]. Depending on the physico-chemical formulation, superstability was achieved by slowing down either one of the three ageing phenomena (e.g. coarsening, using silica nanoparticles and short-chain amphiphiles[83]), or several (all three, using myristic acid-CTACl foams[85,86]). Some dispersions also gel in the continuous phase of the foam[83]. To produce superstable foams with a controlled geometry, procedures such as *in situ* hydrophobisation of particles in microfluidic devices were also reported[84]. To sum things up, achieving foams with good stability properties can imply complex physico-chemical questions that are currently being addressed[83,84].

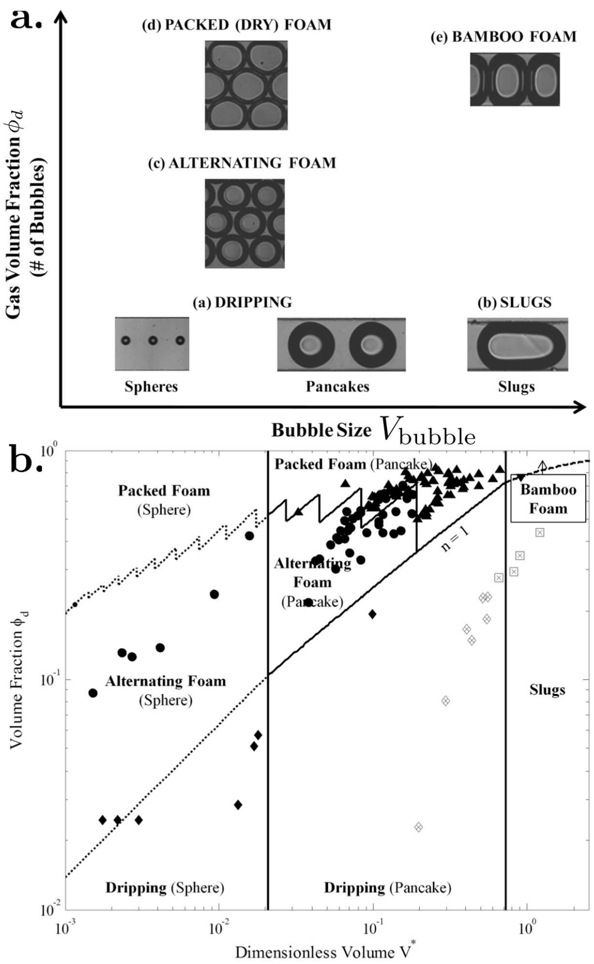

Fig. 11 a: Examples of bubble lattices in the $(V_{\text{bubble}}, \phi_d)$ space. **b:** Mapping of the different foam structures generated in a rectangular microchannel of aspect ratio $\Lambda = H/w = 0.2$. The lines represent the transition between the different regimes, and the symbols account for experimental data: filled symbols are obtained using a flow-focusing device; x-filled symbols are obtained using a co-flow geometry. The symbol shapes correspond to the following regimes: (◇) dripping for spheres and pancakes, (□) slugs, (◯) alternating foam for spheres and pancakes, (△) packed foam for pancakes, (▽) bamboo foam. Reprinted with permission from[78]. Copyright 2012, AIP Publishing LLC.

A different route towards drainage control is to mechanically prevent it by generating flows against the direction of gravity at the film interfaces[87,88]. Examples of this type of strategy at the centimeter scale include electroosmotic[89] or Marangoni flows using photo-surfactants[90,91]. Recent work reported foam drainage control via thermocapillarity in a two-dimensional microfluidic chamber[92]. In this study, a

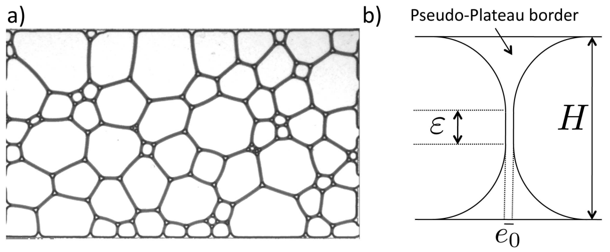

Fig. 12 Geometry of a 2D foam under microconfinement[93]. **a:** the foam appears dry seen from above as the bubbles adopt polygonal shapes; **b:** in a cross-section plane the thin film of height ε and thickness e_0 occupies only a small fraction of the cavity height.

Hele-Shaw cell is placed vertically and the thermocapillary Marangoni stress generated at the air-water interface by a constant temperature gradient is strong enough to counterbalance, or even go against, the *natural* direction imposed by gravity.

3.1.2 Specificities of the microscale. An important question to address is the influence of the confinement below the capillary length on the structure of the foam. Will a microfoam adopt the same geometry as a foam at larger scales, or will the greater pressures involved affect its structure?

In the 2D case, this question was investigated by Marchalot and co-workers[93] by studying the coarsening of a static microfoam, constituted of a single bubble layer squeezed between the two plates of a Hele-Shaw cell, without flow. At the macroscopic scale, the ageing of 2D foams is well-described by Von Neumann's law, which assumes the existence of thin films between bubbles[94]. As smaller bubbles diffuse in larger bubbles, the area A of each bubble evolves with time following $dA/dt = D_{\mathrm{eff}}(n-6)$, where n is the number of sides of the polygonal bubble, and D_{eff} is an effective diffusion coefficient related mainly to the surface tension, the diffusion of gas in the liquid, and the permeability of gas in the liquid films between the bubbles. 2D microfoams undergo a similar time evolution, but much more slowly: D_{eff} was found to be about one order of magnitude smaller than the coefficient measured for similar solutions at larger scales[95]. This difference is due to the height ε of the liquid film between two neighbouring bubbles, represented on Fig. 12. Although the microfoam appears dry in top view, the liquid layer between bubbles is, for the most part, thick enough to slow down significantly the diffusion of the dispersed phase. The height ε over which thin films do form, at the center of the cell, was theoretically estimated to be of order $\sim H/10$[93]. Below the capillary length, the radius of curvature in the pseudo-Plateau borders is set by the confinement: $R = H/2$, which prevents the formation of thin films between bubbles. More precisely, a theoretical study by Gay *et al.* predicts that the radius of curvature in the pseudo-Plateau borders undergoes successive transitions upon progressive increase of the confinement[96]. For constant $(\phi_d, V_{\mathrm{bubble}})$, the pseudo-Plateau borders go through three distinct regimes (E: dry floor tiles, CD, AB: dry pancakes) under progressive squeezing of the foam between the cell plates, see Fig. 13. In this work, the authors predict a film height $\varepsilon \simeq H^2/3R$ provided $H \ll R$. When confined below the capillary length, *i.e.* for both micro- and millifluidics, such a scaling leads to a film height which is less than ∼10 % of the cavity height[96]. Though the two approaches considered different pseudo-Plateau border geometries (circular[93] versus elliptical[96] shape at the interface), they are in good agreement in spite of a slight discrepancy in the film height. Confocal microscopy or tomography might be fruitfully performed to investigate the real geometry of the meniscus.

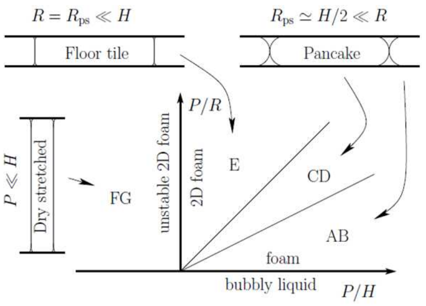

Fig. 13 Log-log representation of the different regimes for a 2D foam squeezed between two solid plates, with low liquid fraction ($\ll 1$), in terms of the bubble perimeter P, the Plateau border radius R and the cell height H. Reprinted from [96] with kind permission from Springer Science and Business Media.

Other specific structures can form only for bubbles smaller than the capillary length. At the macroscale, it is assumed that a 3D wet, monodisperse foam cannot crystallize in bulk from bubbles larger than the capillary length: order prevails only at the boundaries. However, smaller bubbles (∼ 100 μm) placed at a free water/air interface will order and remain wet over $N \sim (l_c/R)^2$ bubble layers, forming substantial microcrystals (R is the bubble radius and l_c the capillary length)[97–99]. Such ordered systems exhibit fcc (face-centered cubic) or bcc (body-centered cubic) structures (see Fig. 14), and a transition from fcc packing at the bottom to a bcc Kelvin structure at the top has been observed in 100-bubble-high foam samples[99]. Soft sphere computer simulations were carried out to provide an image processing tool allowing the interpretation of the observed experimental ordering[99].

Bubbles also self-organize readily under flow when confined to a monolayer; it is then possible to study the diffraction gratings from the bubble lattice. Hashimoto *et al.*[7] developped a microfluidic device able to tune the volume fraction and the size of the bubbles, and observed a transition between disorga-

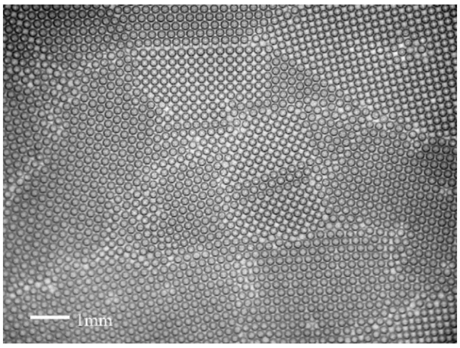

Fig. 14 Top view of a pool of highly monodisperse bubbles (diameter ∼ 250 μm), generated from an aqueous detergent solution. This reveals different grains, ordered in familiar crystalline structures. Reprinted with permission from[99]. Copyright 2007, with permission from Elsevier.

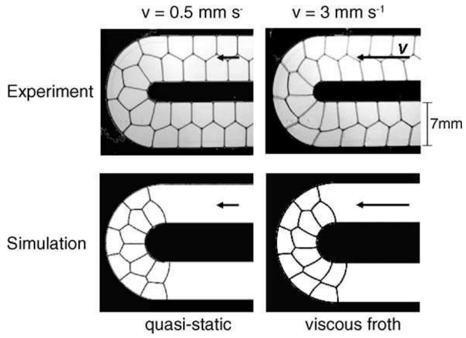

Fig. 15 Top views of a foam flowing around a bend without structural rearrangements. Experimental pictures are compared to computations based on the quasi-static and viscous froth models. Reprinted with permission from[19]. Copyright 2005, with permission from Elsevier.

nized (at low gas volume fraction) and highly-organized flowing lattices, associated with different stabilities of the diffraction pattern. The advantages of such a device are manifold, the most important beeing the tunability of the bubble lattice within one second. Using a 2.5D geometry Malloggi *et al.*[8] were able to produce lattices with droplets ranging from 900 nm to 3 μm.

The development of such highly-controlled materials has important applications in several domains. For instance, microfluidics-generated microfoams were used to template fast and inexpensive scaffolds for cell culture, with uniform pore sizes[9–11]. Such foams constitute a promising building block for this new research field, even though the degree of interconnectivity between pores remains to be improved for tissue engineering applications. The field of micro-fabricated devices for food engineering also expands at a high rate, as the design of novel food microstructures to enhance product quality might require 1 - 100 μm microfoams and microemulsions[100,101].

3.2 Dynamics

When characterizing foam generation processes, several authors measured a different liquid fraction at the outlet than at the inlet, due to viscous dissipation in the lubrications films between the bubbles and the walls[30,32]. This is due to rheological specificities of foams, upon which this section focuses.

3.2.1 Viscous dissipation and foam rearrangements.

The analysis introduced by Bretherton[24], evoked in the first part of this review, was extended to the case of flowing foams where dissipation mainly occurs in the menisci (pseudo-Plateau borders) and in the lubrication films (for immobile interfaces). There is a general consensus that the viscous force scales as $F_D = \lambda U^{\alpha}$, where λ depends on both the interfacial mobility and the liquid fraction, and $1/2 < \alpha < 2/3$ depends on the nature of the surfactant ($\alpha = 2/3$ for a soluble surfactant and $\alpha = 1/2$ for an insoluble surfactant)[102–105]. We have seen in a previous section that the scaling is rather a linear combination of α=(1/3,2/3)[27,67]. These results come from experimental and theoretical studies mostly conducted at the macroscopic scale. However, foam dynamics were investigated at the millimeter scale (with channel depths varying between 0.5 and 1.5 mm, and a channel width of 10 mm) in ordered 2D foams by Drenckhan, Weaire and co-workers, who used two numerical models to rationalize their experimental results[19,97]. At low velocities, a quasi-static model considering a succession of equilibrium states can account for the experimental observations, Fig. 15 (left). However, at larger velocities, the viscous effects become dominant and the structure of the foam is distorted by the drag of the films along the top and bottom walls, Fig. 15 (top right). To account for this drag, the viscous froth model adds to the Laplace pressure a viscous term $\lambda v_{\perp}^{\alpha}$, where $v_{\perp}$ is the velocity normal to the film[106]. The pressure difference between two adjacent bubbles then writes $\Delta P - \gamma\kappa + \lambda v_{\perp}^{\alpha} = 0$, where κ is the local curvature of the film, and α accounts for the surface mobility. In a nutshell, the scaling law for the dissipation is the same for isolated bubbles and foams, though changes in the prefactors arise due to modification of the interface shape (since the meniscus has to be reconnected to the film between adjacent bubbles)[25,77]. As long as the dissipation mainly occurs in the menisci and in the lubrication film (for insoluble surfactants), we do not expect the modification of the foam geometry due to confinement (*i.e.* the absence of films between adjacent bubbles) to affect the different scalings for flowing foams, but this remains to be proved. For instance, the role of the gutters (*i.e.* Plateau borders) might not be negligible in rectangular channels[62,70]. To our knowledge, this was not thoroughly in-

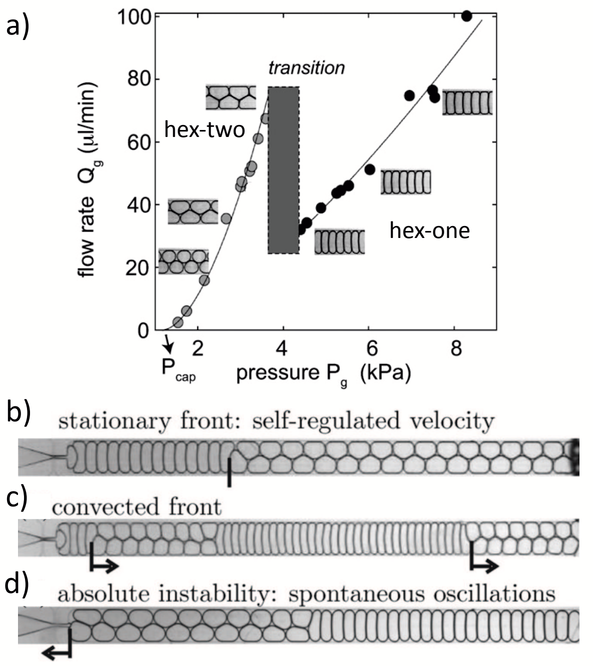

Fig. 16 Transition between two hexagonal structures for flowing crystal. **a:** Flow velocity as a function of the applied gas pressure P_g (at Q_l = 5 μl/min). The intermediate regime was shown to exhibit a plateau in velocity, corresponding to a selfregulated situation where a structure transforms continuously into the other[107]. **b-d:** Intermediate regime with the coexistence of the two lattices. The vertical line represents the position of the front and the arrows its direction of propagation. Reprinted with permission from [30]. Copyright 2009, Royal Society of Chemistry.

vestigated in microfluidic experiments, though Marmottant *et al.* found indirect qualitative agreement[30,31,107].

Weaire *et al.* also predicted dynamical rearrangements in the structure of the foam, known as T1[80,81], above a critical velocity. They correspond to a switch in bubble neighbors and lead to a decrease in the total interface[19,97]. Fig. 16(a) shows, in a microfluidics experiment, a transition between hex-one (metastable state) and hex-two (stable state) lattices produced by a flow-focusing device[30,31,107], associated with a T1 topological rearrangement . We saw that the pressure drop associated to a foam scales as $\Delta P \propto Ca^{\alpha}$, but it also depends on the structure of the foam, and more precisely on L_{proj}, the total length of the films touching the walls projected on a direction transverse to the flow[102]. The hex-one structure thus presents larger resistance to the flow than the hex-two structure, which explains why the hex-one structure cannot be observed at low pressures. Depending on the foam velocity relative to the T1 transformation velocity, three regimes are observed: *i)* stationary instability, see Fig. 16(b); *ii)* advected instability, Fig. 16(c), *iii)* absolute instability, Fig. 16(d).

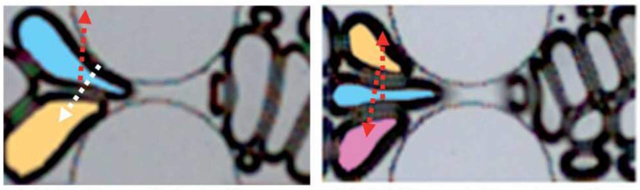
(a) Neighbor-wall pinch-off (b) Neighbor-neighbor pinch-off

Fig. 17 Qualitative indications of the bubble-wall (white dashed arrow) and bubble-bubble (red dashed arrow) interactions experienced by the pinched bubble (blue) in a constricted microchannel. Reprinted with permission from [16]. Copyright 2013, Royal Society of Chemistry.

3.2.2 Flow through constrictions. Another type of microconfinement, particularly relevant to oil-recovery applications, arises when foams flow through constricted pores. Investigating bubble interactions in constricted capillaries, Liontas *et al.*[16] observed two regimes: *i)* neighbor-neighbor pinch-off, where a bubble is squeezed by two neighboring bubbles at a constriction (see Fig. 17(b)), and *ii)* neighbor-wall pinch-off (Fig. 17(a)). In the first case, the neck width decreases almost linearly with time, a behavior reminiscent of bubble pinch-off in a high viscosity external phase (> 100 cP). Conversely, in the second regime, the next width scales like $t^{0.52}$, which is consistent with experiments at low external-phase viscosity (< 10cP). They attribute the high external effective viscosity in the first regime to the fact that the neighboring bubbles are nearly stationary during pinch-off. A good understanding of the dynamics of films in constricted pores would have far-reaching consequences in the substantial field of applications that is Enhanced Oil Recovery (EOR)[17,18,108].

3.3 Discussion

To this day, the topic of foams in microfluidics has been much less addressed in the literature than that of bubbles; moreover, most of these works focus on 2D foams (with the exception of reports on technological achievements, such as 3D bubble lattices). The field of investigation thus remains quite open, all the more so since such studies would be relevant to several domains of application, in static (development of new materials) or flowing conditions (EOR). For instance, the design and high-throughput fabrication of new materials with novel structural properties need complementary studies on 3D foams as well as the scaling-up of the production methods. Perspectives from the fundamental point of vue are further developed in the conclusion.

4 Conclusions

To provide a general picture of the physics at play for dispersed two-phase flows at the microscale, we reviewed fundamental questions such as the mechanisms governing bubble generation in microchannels, the dynamics of a bubble carried by a continuous phase at an imposed flow rate, the geometry of foams confined below the capillary length, the self-organization of bubbles into crystals, and the rheology of confined foams. We stressed the influence of the microconfinement and how it can lead to somewhat counter-intuitive mechanisms, such as the importance of inertial effects in bubble generation. We also pinpointed differences compared to the macroscopic scale, e.g. in the structure of microfoams.

Importantly for practical purposes, we saw that a confined bubble flows at a velocity given by $U/V = 2/(1 + \beta_1\ H/R\ Ca^{-1/3} + \beta_2\ Ca^{-2/3})$, where β_1 and β_2 are constants[67], while the thickness of the lubrication film scales like $h \propto Ca^{2/3}$ with a prefactor depending on the boundary conditions[24,26,27]. Though the dynamics of confined bubbles has been well investigated and some problems can be considered as solved, such as the production of bubbles with a well-controlled size, many issues remain to be addressed. One can cite the influence of intermolecular forces on the lubrication film -which should be felt at the scale of microfluidic devices[28]. Another interesting topic would be the dipolar interaction between two adjacent bubbles, and whether it is modified by the stress-free boundary condition at the interfaces compared to droplets[5,109,110]. Subsidiary studies on the influence of gas compressibility on the dynamics of isolated bubbles or bubble trains would also be instructive[63,65].

In turn, the dynamics of foams at the macroscale is governed by the same scaling laws as the bubble dynamics, since the dissipation occurs mainly in the menisci and lubrication films along the walls; the films between neighboring bubbles appear to play no role. However, the rheology of microfoams could be investigated more thoroughly, as the foam geometry is affected by the microscales. Indeed, working at scales below the capillary length makes it impossible to achieve fully-dry foams since the film height is negligible compared to the radii of the pseudo-Plateau borders -these might be assimilated to gutters and affect the dynamics. This difference might have consequences on the dynamics of microfoams flowing around obstacles, when the pseudo-Plateau borders become tangential to the flow -a situation that has so far only been investigated at the macroscale[105].

At the film level, bubbles and foams pertain to a common field of investigation that focuses on the dynamics at the interface, with and without surfactants. For instance, *rolling* bubbles (see section 2.2.2) undergo interface creation at the bubble front, and simultaneous interface destruction at the rear. The comparative dynamics of bubbles and foams for given surfactant mobilities remain to be explored; the underlying question being the unification of isolated bubble and foam surface rheologies. These results could be further incremented by considering Marangoni effects on the interface dynamics, be they solutal or due to a temperature gradient.

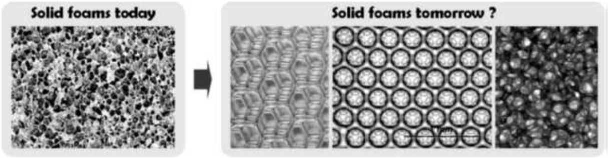

Fig. 18 Thorough understanding of liquid foams pave the way towards porous materials with highly controlled structural properties. Reprinted with permission from[112]. Copyright 2012, with permission from Elsevier.

It is also worth mentioning that once the dynamics of bubbles and foams are established, these objects can be used as tools to investigate physical phenomena at the micro-scale. This is illustrated in two studies previously cited in this review: Rabaud *et al.* used the buoyancy of isolated bubbles to estimate the strength of Bjerkness acoustic forces[66], while Miralles *et al.* opposed thermocapillarity to gravity in a microfoam[92].

We mentioned how microfluidics gives access to structures unachievable at the macroscopic scale: for instance, monodisperse bubbles will self-organize into materials with crystalline structures[97,98]. Technical effort is also being put into the development of materials containing controlled, organized gas micro-inclusions at an intermediate density (between isolated bubbles and close-packed foams): such materials would exhibit interesting acoustic properties. The stability of foams can be enhanced via physico-chemical means, e.g. by adding silica nanoparticles[83,84] or fatty acids[86,111] in the liquid phase, or via hydrodynamic flows countering drainage[92]. The knowledge acquired over the past few decades on foaming and flow chemistry has led to the generation of porous solids with well-controlled morphologies[112] (Fig. 18); microfluidics opens the way towards the development of a new generation of foamy materials with novel structural properties[112].

This work was supported by CNRS, DGA, IPGG Equipex ANR-10-EQPX-34, ESPCI and ANR under the grant 13-BS09-0011-01.

References

1 T. M. Squires and S. R. Quake, Rev. Mod. Phys., 2005, **77**, 977–1026.
2 R. Seemann, M. Brinkmann, T. Pfohl and S. Herminghaus, Rep. Prog. Phys., 2012, **75**, 016601.
3 C. N. Baroud, F. Gallaire and R. Dangla, Lab Chip, 2010, **10**, 2032.
4 D. Bartolo and D. G. A. L. Aarts, Soft Matter, 2012, **8**, 10530.
5 T. Beatus, R. H. Bar-Ziv and T. Tlusty, Phys. Rep., 2012, **516**, 103–145.

6 V. Leroy, A. Strybulevych, M. G. Scanlon and J. H. Page, Eur. Phys. J. E, 2009, **29**, 123–130.

7 M. Hashimoto, B. Mayers, P. Garstecki and G. M. Whitesides, Small, 2006, **2**, 1292–1298.

8 F. Malloggi, N. Pannacci, R. Attia, F. Monti, P. Mary, H. Willaime, P. Tabeling, B. Cabane and P. Poncet, Langmuir, 2010, **26**, 2369–2373.

9 C.-C. Wang, K.-C. Yang, K.-H. Lin, H.-C. Liu and F.-H. Lin, Biomaterials, 2011, **32**, 7118–7126.

10 C. Colosi, M. Costantini, A. Barbetta, R. Pecci, R. Bedini and M. Dentini, Langmuir, 2013, **29**, 82–91.

11 K.-Y. Chung, N. C. Mishra, C.-C. Wang, F.-H. Lin and K.-H. Lin, Biomicrofluidics, 2009, **3**, 022403.

12 S.-L. Lin, T.-Y. Lin and M.-R. Fuh, Electrophoresis, 2013, 1–10.

13 K. Ferrara, R. Pollard and M. Borden, Annu. Rev. Biomed. Eng., 2007, **9**, 415–447.

14 E. Stride and N. Saffari, Proc. Inst. Mech. Eng. H J. Eng. Med., 2003, **217**, 429–447.

15 J. C. Jokerst, J. M. Emory and C. S. Henry, The Analyst, 2012, **137**, 24.

16 R. Liontas, K. Ma, G. J. Hirasaki and S. L. Biswal, Soft Matter, 2013, **9**, 10971.

17 R. Farajzadeh, A. Andrianov and P. L. J. Zitha, Ind. Eng. Chem. Res., 2010, **49**, 1910–1919.

18 G. Hirasaki, C. Miller and M. Puerto, SPE Journal, 2011, **16**, 889–907.

19 W. Drenckhan, S. J. Cox, G. Delaney, H. Holste, D. Weaire and N. Kern, Colloids Surf., A, 2005, **263**, 52–64.

20 V. Leroy, A. Bretagne, M. Fink, H. Willaime, P. Tabeling and A. Tourin, Appl. Phys. Lett., 2009, **95**, 171904.

21 T. Cubaud, U. Ulmanella and C.-M. Ho, Fluid Dynamics Research, 2006, **38**, 772–786.

22 L. Shui, J. C. T. Eijkel and A. van den Berg, Sensors and Actuators B: Chemical, 2007, **121**, 263–276.

23 J. M. Köhler and B. P. Cahill, Micro-Segmented Flow - Applications in Chemistry and Biology, Springer, 2014.

24 F. P. Bretherton, J. Fluid Mech., 1961, **10**, 166–188.

25 D. Burgess and M. R. Foster, Phys. Fluids A, 1990, **2**, 1105–1117.

26 A. Q. Shen, B. Gleason, G. H. McKinley and H. A. Stone, Phys. Fluids, 2002, **14**, 4055–4068.

27 I. Cantat, Phys. Fluids, 2013, **25**, 031303.

28 G. F. Teletzke, H. T. Davis and L. Scriven, Revue de Physique Appliquée, 1988, **23**, 989–1007.

29 P. Guillot, A. Colin and A. Ajdari, Phys. Rev. E, 2008, **78**, 016307.

30 P. Marmottant and J.-P. Raven, Soft Matter, 2009, **5**, 3385.

31 J.-P. Raven and P. Marmottant, Phys. Rev. Lett., 2006, **97**, 154501.

32 P. Garstecki, I. Gitlin, W. DiLuzio, G. M. Whitesides, E. Kumacheva and H. A. Stone, Appl. Phys. Lett., 2004, **85**, 2649–2651.

33 P. Garstecki, M. J. Fuerstman, H. A. Stone and G. M. Whitesides, Lab Chip, 2006, **6**, 437–446.

34 J. H. Xu, S. W. Li, Y. J. Wang and G. S. Luo, Appl. Phys. Lett., 2006, **88**, 133506.

35 M. De Menech, P. Garstecki, F. Jousse and H. A. Stone, J. Fluid Mech., 2008, **595**, 141–161.

36 V. van Steijn, C. R. Kleijn and M. T. Kreutzer, Lab Chip, 2010, **10**, 2513.

37 P. Garstecki, M. J. Fuerstman and G. M. Whitesides, Phys. Rev. Lett., 2005, **94**, 234502.

38 S. L. Anna, N. Bontoux and H. A. Stone, Appl. Phys. Lett., 2003, **82**, 364–366.

39 P. Guillot, A. Colin, A. S. Utada and A. Ajdari, Phys. Rev. Lett., 2007, **99**, 104502.

40 W. van Hoeve, B. Dollet, J. M. Gordillo, M. Versluis, L. van Wijngaarden and D. Lohse, EPL (Europhysics Letters), 2011, **94**, 64001.

41 T. Cubaud, M. Tatineni, X. Zhong and C.-M. Ho, Phys. Rev. E, 2005, **72**, 037302.

42 M. Stoffel, S. Wahl, E. Lorenceau, R. Höhler, B. Mercier and D. E. Angelescu, Phys. Rev. Lett., 2012, **108**, 198302.

43 B. Dollet, W. van Hoeve, J.-P. Raven, P. Marmottant and M. Versluis, Phys. Rev. Lett., 2008, **100**, 034504.

44 W. van Hoeve, B. Dollet, M. Versluis and D. Lohse, Phys. Fluids, 2011, **23**, 092001.

45 P. Garstecki, A. M. Ganan-Calvo and G. M. Whitesides, Bulletin of the Polish Academy of Sciences. Technical Sciences, 2005, **Vol. 53**, 361–372.

46 A. M. Leshansky and L. M. Pismen, Phys. Fluids, 2009, **21**, 023303.

47 A. M. Leshansky, S. Afkhami, M.-C. Jullien and P. Tabeling, Phys. Rev. Lett., 2012, **108**, 264502.

48 M.-C. Jullien, M.-J. T. M. Ching, C. Cohen, L. Ménétrier and P. Tabeling, Phys. Fluids, 2009, **21**, 072001.

49 D. Langevin, ChemPhysChem, 2008, **9**, 510–522.

50 D. Langevin, Annu. Rev. Fluid Mech., 2014, **46**, 47–65.

51 J.-C. Baret, Lab Chip, 2012, **12**, 422.

52 K. J. Stebe and D. Barthes-Biesel, J. Fluid Mech., 1995, **286**, 25–48.

53 G. Taylor and P. G. Saffman, Q J Mechanics Appl Math, 1959, **12**, 265–279.

54 L. D. Landau and B. Levich, Acta Physicochimica USSR, 1942, **17**, 42.

55 S. R. Hodges, O. E. Jensen and J. M. Rallison, J. Fluid Mech., 2004, **501**, 279–301.

56 B. V. Derjaguin, Acta Physicochimica USSR, 1943, **20**, 349.

57 P. Garstecki, M. A. Fischbach and G. M. Whitesides, Appl. Phys. Lett., 2005, **86**, 244108.

58 T. C. Thulasidas, M. A. Abraham and R. L. Cerro, Chem. Eng. Sci., 1999, **54**, 61–76.

59 C.-W. Park and G. M. Homsy, J. Fluid Mech., 1984, **139**, 291–308.

60 N. D. Denkov, S. Tcholakova, K. Golemanov, V. Subramanian and A. Lips, Colloids Surf., A, 2006, **282**, 329–347.

61 J. Ratulowski and H.-C. Chang, Phys. Fluids A, 1989, **1**, 1642–1655.

62 H. Wong, C. J. Radke and S. Morris, J. Fluid Mech., 1995, **292**, 71–94.

63 T. Cubaud and C.-M. Ho, Phys. Fluids, 2004, **16**, 4575–4585.

64 N. Quennouz, M. Ryba, J.-F. Argillier, B. Herzhaft, Y. Peysson and N. Pannacci, Oil & Gas Science and Technology-Rev. IFP Energies Nouvelles, 2014.

65 B. Scheid: private communication.

66 D. Rabaud, P. Thibault, J.-P. Raven, O. Hugon, E. Lacot and P. Marmottant, Phys. Fluids, 2011, **23**, 042003.

67 R. Dangla, PhD thesis, Ecole Polytechnique, 2012.

68 S. R. K. Maruvada and C.-W. Park, Phys. Fluids, 1996, **8**, 3229–3233.

69 A. R. Kopf-Sill and G. M. Homsy, Phys. Fluids, 1988, **31**, 18–26.

70 M. J. Fuerstman, A. Lai, M. E. Thurlow, S. S. Shevkoplyas, H. A. Stone and G. M. Whitesides, Lab Chip, 2007, **7**, 1479–1489.

71 M. Muradoglu and H. A. Stone, J. Fluid Mech., 2007, **570**, 455–466.

72 R. Dangla, F. Gallaire and C. N. Baroud, Lab Chip, 2010, **10**, 2972–2978.

73 B. Selva, J. Marchalot and M.-C. Jullien, J. Micromech. Microeng., 2009, **19**, 065002.

74 B. Selva, I. Cantat and M.-C. Jullien, Phys. Fluids, 2011, **23**, 052002.

75 M. Prakash and N. Gershenfeld, Science, 2007, **315**, 832–835.

76 W. Choi, M. Hashimoto, A. K. Ellerbee, X. Chen, K. J. M. Bishop, P. Garstecki, H. A. Stone and G. M. Whitesides, Lab Chip, 2011, **11**, 3970–3978.

77 A. Saugey, W. Drenckhan and D. Weaire, Phys. Fluids, 2006, **18**, 053101.

78 S. M. Vuong and S. L. Anna, Biomicrofluidics, 2012, **6**, 022004.

79 M. Hashimoto, P. Garstecki and G. M. Whitesides, Small, 2007, **3**, 1792–1802.

80 D. L. Weaire and S. Hutzler, The physics of foams, Clarendon Press,

Oxford; New York, 1999.

81 I. Cantat, S. Cohen-Addad, F. Elias, F. Graner, R. Höhler and O. Pitois, Foams: Structure and Dynamics, Oxford University Press, 2013.

82 A. D. Dinsmore, M. F. Hsu, M. G. Nikolaides, M. Marquez, A. R. Bausch and D. A. Weitz, Science, 2002, **298**, 1006–1009.

83 L. R. Arriaga, W. Drenckhan, A. Salonen, J. A. Rodrigues, R. Iñiguez Palomares, E. Rio and D. Langevin, Soft Matter, 2012, **8**, 11085.

84 E. Rio, W. Drenckhan, A. Salonen and D. Langevin, Adv. Colloid Interface Sci., 2014, **205**, 74–86.

85 A. Stocco, D. Carrière, M. Cottat and D. Langevin, Langmuir, 2010, **26**, 10663–10669.

86 D. Varade, D. Carrière, L. R. Arriaga, A.-L. Fameau, E. Rio, D. Langevin and W. Drenckhan, Soft Matter, 2011, **7**, 6557.

87 S. A. Koehler, S. Hilgenfeldt and H. A. Stone, Langmuir, 2000, **16**, 6327–6341.

88 A. Saint-Jalmes, Soft Matter, 2006, **2**, 836.

89 O. Bonhomme, O. Liot, A.-L. Biance and L. Bocquet, Phys. Rev. Lett., 2013, **110**, 054502.

90 E. Chevallier, A. Mamane, H. A. Stone, C. Tribet, F. Lequeux and C. Monteux, Soft Matter, 2011, **7**, 7866.

91 E. Chevallier, C. Monteux, F. Lequeux and C. Tribet, Langmuir, 2012, **28**, 2308–2312.

92 V. Miralles, B. Selva, I. Cantat and M.-C. Jullien, Submitted, **XXX**, XXX.

93 J. Marchalot, J. Lambert, I. Cantat, P. Tabeling and M.-C. Jullien, EPL (Europhysics Letters), 2008, **83**, 64006.

94 J. von Neumann, American Society for Metals, Cleveland, 1952, 108.

95 H. M. Princen, J. T. G. Overbeek and S. G. Mason, J. Colloid Interface Sci., 1967, **24**, 125–130.

96 C. Gay, P. Rognon, D. Reinelt and F. Molino, Eur. Phys. J. E, 2011, **34**, 1–11.

97 D. Weaire and W. Drenckhan, Adv. Colloid Interface Sci., 2008, **137**, 20–26.

98 D. Weaire, S. T. Tobin, A. J. Meagher and S. Hutzler, Foam Engineering, John Wiley & Sons, Ltd, 2012, pp. 5–26.

99 A. van der Net, G. W. Delaney, W. Drenckhan, D. Weaire and S. Hutzler, Colloids Surf., A, 2007, **309**, 117–124.

100 O. Skurtys and J. M. Aguilera, Food Biophysics, 2008, **3**, 1–15.

101 E. Hughes, A. A. Maan, S. Acquistapace, A. Burbidge, M. L. Johns, D. Z. Gunes, P. Clausen, A. Syrbe, J. Hugo, K. Schroen, V. Miralles, T. Atkins, R. Gray, P. Homewood and K. Zick, J. Colloid Interface Sci., 2013, **389**, 147–156.

102 I. Cantat, N. Kern and R. Delannay, EPL (Europhysics Letters), 2004, **65**, 726.

103 N. D. Denkov, V. Subramanian, D. Gurovich and A. Lips, Colloids Surf., A, 2005, **263**, 129–145.

104 E. Terriac, J. Etrillard and I. Cantat, EPL (Europhysics Letters), 2006, **74**, 909.

105 B. Dollet, F. Elias, C. Quilliet, A. Huillier, M. Aubouy and F. Graner, Colloids Surf., A, 2005, **263**, 101–110.

106 N. Kern, D. Weaire, A. Martin, S. Hutzler and S. Cox, Phys. Rev. E, 2004, **70**, 041411.

107 J.-P. Raven and P. Marmottant, Phys. Rev. Lett., 2009, **102**, 084501.

108 K. Ma, R. Liontas, C. A. Conn, G. J. Hirasaki and S. L. Biswal, Soft Matter, 2012, **8**, 10669–10675.

109 B. Shen, M. Leman, M. Reyssat and P. Tabeling, Exp. Fluids, 2014, in press.

110 W. E. Uspal and P. S. Doyle, Soft Matter, 2012, **8**, 10676–10686.

111 A.-L. Fameau, A. Saint-Jalmes, F. Cousin, B. Houinsou Houssou, B. Novales, L. Navailles, F. Nallet, C. Gaillard, F. Boué and J.-P. Douliez, Angew. Chem., Int. Ed., 2011, **50**, 82648269.

112 A. Testouri, L. R. Arriaga, C. Honorez, M. Ranft, J. Rodrigues, A. van der Net, A. Lecchi, A. Salonen, E. Rio, R. M. Guillermic, D. Langevin and W. Drenckhan, Colloids Surf., A, 2012, **413**, 17–24.